Dual-band metamaterial absorber with a low-coherence composite cross structure in mid-wave and long-wave infrared bands

ENZHU HOU,[1] ZHENG QIN,[2,3] ZHONGZHU LIANG,[1,2,3,*] DEJIA MENG,[2] XIAOYAN SHI,[2,3] FUMING YANG,[2,3] WENJUN LIU,[2,3] HUA LIU,[1] HAIYANG XU,[1] DAVID R. SMITH,[4] AND YICHUN LIU[1]

[1]*Center for Advanced Optoelectronic Functional Materials Research and Key Laboratory of UV Light-Emitting Materials and Technology of Ministry of Education, College of Physics, Northeast Normal University, Changchun 130024, China*

[2]*State Key Laboratory of Applied Optics, Changchun Institute of Optics, Fine Mechanics and Physics, Chinese Academy of Sciences, Changchun, Jilin 130033, China*

[3]*University of the Chinese Academy of Sciences, China*

[4]*Center for Metamaterials and Integrated Plasmonics, Duke University, P.O. Box 90291, Durham, North Carolina 27708, USA*

[*]liangzz@nenu.edu.cn

Abstract: The atmospheric window in the infrared (IR) band primarily consists of mid-wave (MWIR, 3-5 μm) and long-wave IR (LWIR, 8-12 μm) bands, also known as the working bands in most of the IR devices. The main factor affecting the device capability includes the absorption efficiency, hence, the absorption material. Herein, a dual-band absorber based on the composite cross structure (CCS) in both MWIR and LWIR bands was proposed, with absorption peaks of 4.28 μm and 8.23 μm. The obtained absorber is with high scalability in the MWIR and LWIR region respectively by tuning the structural parameters. A quadrupole polarization model is proposed for further understanding of the uneven distribution of electromagnetic field that was caused by the change of the center spacing of the embedded structure. Meanwhile, it was shown that the two absorption peaks exhibited good incident angle stability. In addition, as the incident angle of the TM mode increases, a waveguide is formed between the embedded structure and the surface structure, leading to another strong absorption in the LWIR band. The results showed that absorption increases as the incident angle increases. The proposed absorber can be a good candidate for applications in thermal emission, detection and solar energy harvesting.

1.   Introduction

In recent years, metamaterial absorbers have been widely used and rapidly developed because of their ability to almost perfectly absorb the specific wavelength of electromagnetic waves [1,2]. They exhibit important application potentials in the fields of detection [3], sensing [4,5], emission [6–10], and imaging [11–13]. By reasonably designing structure parameters, composition materials, surface patterns, and other characteristic factors of the absorber structure, the maximum possible electromagnetic energy was coupled to achieve high absorption at a specific wavelength [14–16]. So far, the research on these absorbers in various wave bands such as microwave [17,18], THz [19–22], long-wave infrared (LWIR) [23], mid-wave infrared (MWIR) [9,24,25], and visible-near-infrared [10,26,27] bands has been carried out. According to Wien's law, the electromagnetic radiation bands of normal-temperature objects and high-temperature objects include the MWIR and LWIR bands, respectively. The operating band of most of the thermal imaging systems includes MWIR or the LWIR band. However, presently, there are a few relevant research studies on both MWIR and LWIR absorbers. In comparison to the absorption

of a single band, the absorption of both MWIR and LWIR bands can be realized at the same time, which can achieve information complementation, increase target information and reduce the false alarm rate caused by the detector in applications such as early warning and search.

Generally, the method to realize the dual-band, the multi-band, or the broadband absorber can be divided into two types of vertical stacking and horizontal integration. Vertical stacking achieves multi-band or broadband absorption by stacking multiple layers of metal-insulator (MI) structures [18,20,26]. A dual-band metamaterial absorber in the MWIR band was designed by using the stack of two pairs of circular-patterned MI [28]. At the same time, horizontal integration achieved multi-band or broadband absorption by designing the resonance units of different structures or integrating the resonance units of different sizes on the same dielectric plane [14,29]. A narrow-band MWIR metamaterial absorber was experimentally realized, and multiple metamaterial sublattices were further developed to realize a dual-band absorber in the MWIR band [14].

These methods have certain limitations to obtain dual-band absorbers in both MWIR and LWIR bands. Stacking multiple MI structures to achieve a multi-band absorber design makes the absorber structure thicker and thereby increases the difficulty of micro-nano processing and reduces the stability of the incident angle of the absorber. At the same time, it is difficult for the stacked structure to adjust the single absorption peak of multi-band absorption. In the horizontal integration method, due to the impedance matching conditions of the metal-insulator-metal (MIM)-stacked structure, the thickness of the insulator dielectric layer has a specific relationship with the characteristic size of the surface resonance structure. It is also difficult to simultaneously achieve the high absorption of two peaks with large spacing. Therefore, neither of these two methods are considered suitable to obtain a dual-band absorber in the LWIR and MWIR bands.

In this paper, a novel composite cross structure (CCS) was designed to achieve a strong absorption at 4.28 μm and 8.23 μm in the MWIR and LWIR bands, with 98.2% and 99.5% absorption, respectively. According to the impedance matching conditions of the metamaterial absorber, different sizes of absorbers achieve near-perfect absorption accompanied by different dielectric thicknesses. To achieve dual-band high absorption in the MWIR and LWIR bands, a small-sized cross structure to be embedded in the insulator dielectric layer of the MIM-stacked structure with a cross pattern was designed. The cross structure of the resonance unit displayed a small geometric duty ratio, and the electromagnetic interaction between the surface structure and the embedded structure was reduced as much as possible. The absorber showed good geometric adjustment capability. The design of the structural feature sizes (L_1, L_2, and D) could realize the regular adjustment of the MWIR or the LWIR absorption. The quadrupole polarization resonant model was proposed to analyze the polarization phenomenon of the localized surface plasmon (LSP). The absorption mechanism and influencing factors of the single surface cross MIM-stacked structure at 4.28 μm in the MWIR band were analyzed. Besides, the influence of the incidence angle in the TE mode and TM mode on the absorption characteristics of the absorber was also discussed.

2. Design and result

Most metamaterial absorber structures are composed of MIM stacks. The top layer is called the periodic metal resonator, and the middle layer and the bottom layer are called the insulator dielectric and the metal reflective substrate, respectively. Based on the loss theory of metal materials, when the thickness of the metal plate is greater than the penetration depth of the metal at a certain frequency, the metal plate can be approximated as a perfect reflection layer. This occurs due to the substrate metal of the MIM-stacked, that is, when the transmission, $T = 0$. According to the equivalent dielectric theory [30–32], the reflection of the equivalent dielectric on the incident electromagnetic wave can be expressed as $R = (Z_{eff} - Z_0) / (Z_{eff} + Z_0)$, where Z_{eff} is the equivalent impedance of the MIM-stacked structure and Z_0 is the free space impedance.

The reflection indicates the matching degree of the structural equivalent impedance and the free space impedance. When $Z_{\text{eff}} = Z_0$, the reflectivity $R = 0$, theoretically achieving the perfect absorption in a specific frequency band.

Based on the finite difference time domain method, a sub-wavelength dual-band metamaterial absorber was designed to achieve high absorption in the MWIR and LWIR bands. Figure 1 shows the schematic of the proposed structure, and four small-sized cross structures embedded in the insulator dielectric layer of the MIM-stacked structure with a cross structure on the surface. The composite MIM-stacked cross structure achieved high absorption in the MWIR and LWIR bands. The absorber is a periodic array in the *x* and *y* directions, and the period (*P*) was estimated at 4 μm. The thickness (*d*) of the substrate metal, embedded cross structure (ECS) and surface cross structure (SCS) were Au at 0.05 μm. The distance (*D*) between the four ECSs and the horizontal center axis ($z = 0$ μm) of the structure was estimated at 1 μm. The characteristic size of the metamaterial absorber structure is the main factor that affects the absorption peak position, and the size of the cross structure is very important to achieve dual-band absorption in the MWIR and LWIR bands. By using the optimized design, the characteristic sizes of the cross structure were as follows: L_1=2.8 μm, l_1=0.5 μm, L_2=0.9 μm, and l_2=0.2 μm. Further, Al_2O_3 with a dielectric thickness (*H*) of 0.3 μm was used to achieve dual-band impedance matching, and the vertical distance (*h*) between the cross structure embedded in the dielectric and the base metal was 0.2 μm. The optical constants of Au and Al_2O_3 used in the calculation were extracted from the data reported by Palik [33,34], and the boundary conditions in the x and y directions are periodic and the boundary conditions in the z direction are perfectly matched layers.
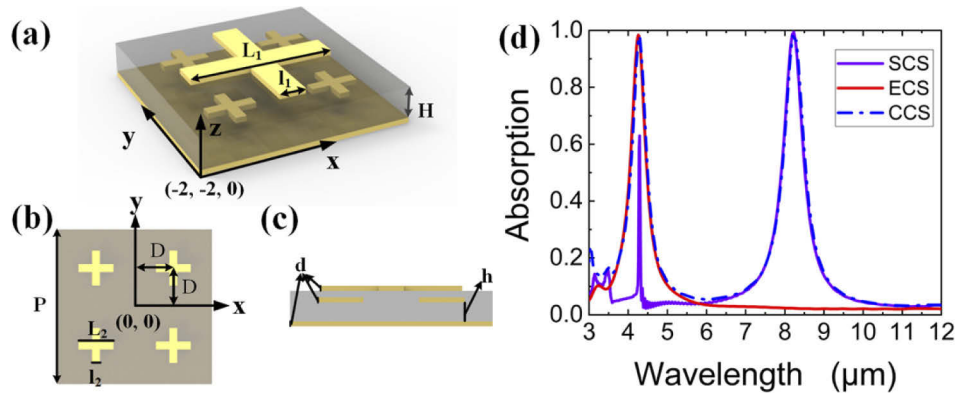

Fig. 1. Schematic diagram of CCS: (a) three-dimensional structure, (b) cross-sectional view of embedded structure, (c) cross-sectional view of y = 1 μm, and (4) absorption spectrum

The absorption spectrum of the absorber is shown in Fig. 1(d). The results showed that CCS achieved a high absorption of 98.2% at 4.28 μm in the MWIR band and 99.5% at 8.23 μm in the LWIR band. The same could also be observed from the absorption line of the SCS *only*, having an absorption peak at 4.29 μm in the MWIR band. The absorption peak shows a narrow absorption bandwidth and poor acquisition and processing capabilities for thermal radiation information. Therefore, by using the dimensional characteristics and optimized design of the metamaterial absorber, four small-sized cross structures were embedded in the dielectric layer to compensate for the MWIR absorption of the SCS. The absorption of the ECS was indicated by the red curve, as shown in Fig. 1(d).

Furthermore, the electric-field and magnetic-field distributions were investigated to better understand the absorption mechanism. The cross-sectional distribution of the electromagnetic field of the composite structure is shown in Fig. 2. The LWIR absorption depends on the SCS. It could be seen from Fig. 2(a) and (b) that the electric field at the LWIR absorption peak at

8.23 µm was mainly concentrated at the edge of the interface between the surface structure and the insulator dielectric, caused by the enhancement of the localized electromagnetic field of the surface plasmon. The LSP excitation leads to the coupling of the magnetic field with the dielectric [35,36]. It was also observed from Fig. 2(b) that the magnetic field was mainly concentrated in the dielectric layer directly below the SCS. The high absorption at 4.28 µm in the MWIR band mainly depended on the cross structure embedded in the dielectric, as observed from the electromagnetic-field distribution diagram shown in Fig. 2(c) and (d). Under the irradiation of incident electromagnetic waves, the LSP of the embedded structure was excited to concentrate the electric field at both sides of the embedded structure. Moreover, the magnetic field was coupled to the dielectric area where the surface pattern was directly opposite to and the substrate.
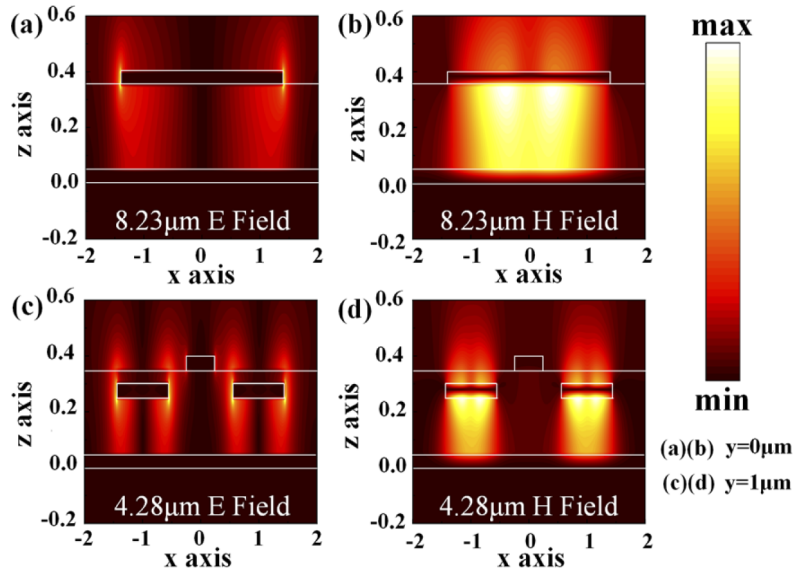

Fig. 2. (a) Electric field and (b) magnetic field distribution at LWIR absorption peak, (c) electric field and (d) magnetic field distribution at the MWIR absorption peak

3. Absorber performance discussion

3.1. Mid-wave narrow-band absorption analysis of the SCS

It could be seen from Fig. 1(d) that in the absorption line of the SCS, in addition to the absorption peak of the LWIR band, a very narrow-band peak in the MWIR band was also observed. The electromagnetic-field distribution diagram of the absorption peak is shown in Fig. 3(a) and (b). The electric field is locally concentrated on both sides of the surface metal cross resonator. The magnetic field in the dielectric is not only distributed in the dielectric area covered by the resonance structure but also in the insulator dielectric area not covered by the resonator. Based on the analysis of the electromagnetic-field distribution, the narrow-band absorption was achieved by the propagating surface plasmon (PSP) resonance excited by the SCS [35,36].

The absorption peak is related to the dielectric thickness of the insulator, as shown in Fig. 3(c). As the thickness of the dielectric changed from 0.30 µm to 0.40 µm, the absorption peak position shifted, from 4.29 µm to 4.46 µm, and its absorption was also increased. The absorption peak can also be tuned by varying the period P of the CCS array. Figure 3(d) shows the absorption efficiency as a function of the period. With the increase in P, the PSP resonance wavelength shifted to a longer wavelength, whereas the LSP resonance wavelength remained constant. The
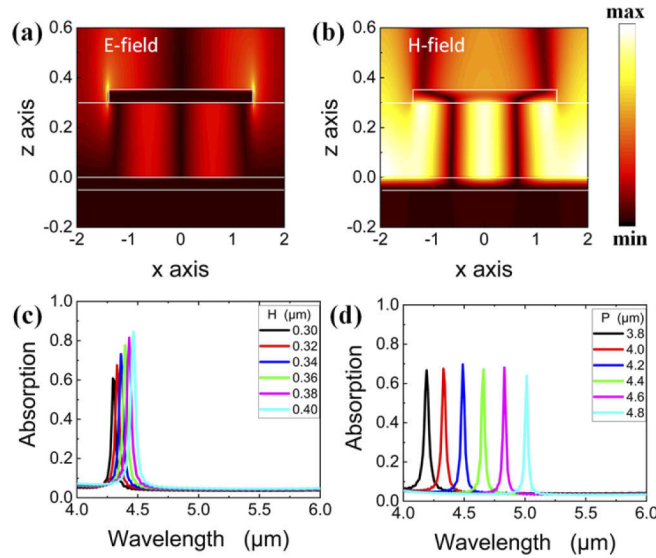
Fig. 3. (a) Electric field and (b) magnetic field distribution of the SCS at the absorption peak of the MWIR at 4.29 μm, and structural parameters (c) thickness of the dielectric, and (d) the effect of the structural period on the IR absorption peak of the wave in the SCS.

relation between the PSP wavelength and period P could be explained by the PSP dispersion relationship, given by the following equation:

$$k_{psp} = \frac{2\pi}{\lambda_0} \times sin\theta_{inc} + \frac{2\pi}{P} \times m \tag{1}$$

where k_{psp} is the PSP wave vector along the surface of Au-SiO$_2$, λ_0 is the wavelength in free space, θ_{inc} is the incident angle, and m is an integer. As the period changes from 3.8 μm to 4.8 μm, the absorption peak increases with the period, and its position changes from 4.19 μm to 5.01 μm, relatively susceptible to the period, however, the change in absorption is not obvious. The full width at half maximum of the narrow-band absorption peak was about 0.035 μm. The study of narrow-band absorption is of great significance in the application of high-sensitivity sensing and other application fields [37]. The period-sensitive characteristics assist modulating the absorption peak, which is helpful for its applications in devices of various bands.

3.2. Size modulation analysis of the composed cross structure

The near-unity absorption of the dual-band metamaterial absorbers is achieved by using the LSP resonance. The absorption frequency is mainly related to the feature size of the SCS, and the absorption peak position of the absorber can be modulated by changing the feature size of the structure. There is no mutual relationship between the absorption of the SCS and the ECS, since the cross structure has a small geometric duty ratio and the very concentrated electromagnetic field generated in the dielectric. By changing the feature sizes L_1 and L_2 of the SCS and ECS, the absorption can be changed. As L_1 increased from 2.4 μm to 3.2 μm, with an interval of 0.2 μm, the absorption peak of the LWIR shifted from 7.49 μm to 8.92 μm (Fig. 4). Also, as the feature size L_2 of the embedded structure increased from 0.8 μm to 1 μm and the changing unit was equal to 0.05 μm, the MWIR absorption peak exhibited a redshift from 3.89 μm to 4.67 μm. The respective changes did not affect each other, and thus independent adjustment could be achieved.
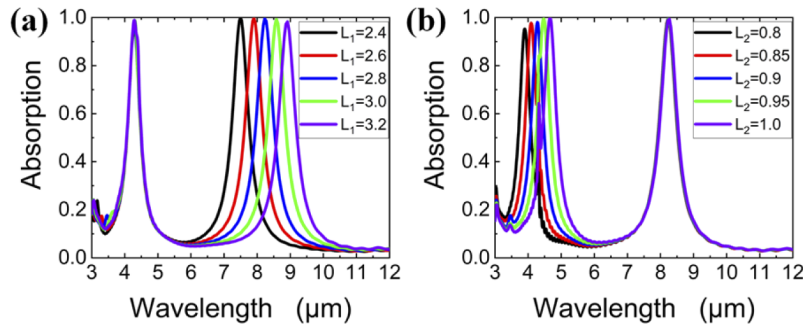
Fig. 4. Modulation of the LWIR and MWIR resonance absorption peaks.

3.3. Effect of the center distance of the embedded structure on absorption

The effect of the distance D between the center of the ECS and the axis ($x = 0$ or $y = 0$) was analyzed to determine whether the structures interact with each other as the parameters change. Figure 5(a) and (b) shows the changes in the absorption of the MWIR and LWIR bands, respectively. When D was 1 µm, only one absorption peak was observed, whereas it was not equal to 1, two absorption peaks were formed (Fig. 5(a)). This could be attributed to the decrease in the distance between the ECSs with the coupling between the adjacent ECSs. According to the periodic boundary conditions, when there is no other interference and $D_1 + D_2 = 2$ µm, the absorption of D_1 and D_2 should be the same. However, contradictory results were observed in Fig. 5, depicting the presence of other interferences besides the interaction between the ECSs. Figure 5(b) shows the variation of LWIR with the change in D; when D was greater than 1 µm, the LWIR absorption peak did not change, while when it was less than 1 µm, the distance between the surface structure and the embedded structure became smaller, causing an electromagnetic effect between the surface structure and the embedded structure, shifting the absorption peak of the LWIR band.
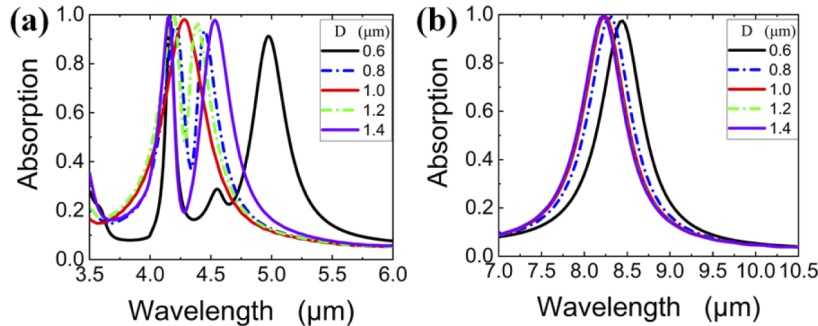

Fig. 5. Modulation of the distance of the central axis of the embedded structure.

To further analyze the variation of the absorption spectrum with the change in the center distance D, the electromagnetic-field distribution of the MWIR absorption peak position at $D = 1.4$ µm and 0.6 µm is shown in Fig. 6. When $D = 1.4$ µm, the electromagnetic-field distribution at the two MWIR absorption peaks at 4.17 µm and 4.53 µm is shown in Fig. 6(a), (b), (f) and (g) (equivalent to no SCS affecting the absorption of the MWIR when $D = 0.6$ µm). Due to the change in the center distance of the embedded structure, the intrinsic resonance equilibrium state produces polarization, thereby changing the number of absorption peaks from one to two, respectively, resulting in a blueshift and redshift. From the electric-field distribution shown in Fig. 6(a) and (f), it could be understood that the reason for the strong absorption was the excitation

of the LSP resonance, but the electromagnetic field intensity at both ends of a single embedded structure is different. The magnetic-field distribution in Fig. 6(f) and (g) showed that the outer side of the magnetic field at 4.17 µm was stronger than the inner side corresponding to the outer polarization coupling mode, and the inner side of the magnetic field at 4.53 µm was stronger than the outer side corresponding to the inner polarization coupling mode. When $D = 0.6$ µm, the center distance D became smaller. The embedded structure existed in the plasmon resonance coupling field of the surface structure and was subject to electromagnetic influence. The two absorption peaks generated by the external and internal polarization coupling resonance shifted to 4.19 µm and 4.97 µm, respectively. As D becomes smaller, the interaction between the internal polarization mode and the SCS coupling field becomes stronger. It could be seen from the fact that surface plasmons are only produced in TM mode (Fig. 6(c), (e), (h) and (j)), the resonance in the y-direction was excited by the coupling field of the surface structure. The absorption peak at 4.59 µm was due to the reduced distance D from the center of the embedded structure, which limits the propagating surface plasmon resonance mode. Therefore, the electric- and magnetic-field distributions in Fig. 6(d) and (i) showed a strong resonance near $y = 0$.
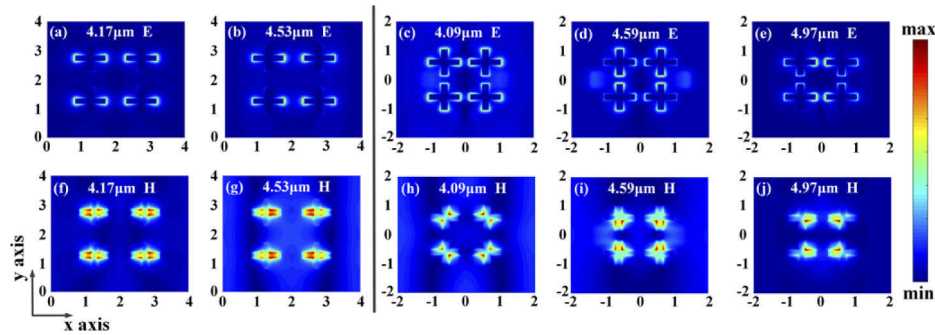

Fig. 6. The electromagnetic-field distribution corresponding to the absorption peaks in the MWIR band, when the center distance $D = 0.6$ µm ((c), (d), (e), (h), (i), (j)) and D = 1.4 µm ((a), (b), (f), (g)).

In classical mechanics, two objects that do simple harmonic motion (SHM) are connected together to form a coupled resonant subsystem. The coupled harmonic oscillator model can be used to describe a variety of coupled systems and physical phenomena, such as electromagnetically induced transparency. The surface-enhanced infrared absorption can also be explained intuitively using this model. According to the electromagnetic-field distribution of the ECS absorber, we established a quadrupole polarization model of the internal and external coupling plasmon resonances, as shown in Fig. 7 (The spherical radius indicates that the electromagnetic field is strong or small, and the sign indicates that the z-axis component of the electric field is in the opposite direction.). Figure 7(a) shows the equilibrium state when $D = 1$ µm, which can be explained with a periodic 1D dipole array. To understand the internal and external plasmon polarization resonances more intuitively, we equated the electromagnetic-field distribution of the embedded structure at $D = 1.4$ µm with the quadrupole resonance model as shown in Fig. 7(b) and (c). Figure 7(b) shows the internal coupling, with a wavelength of 4.17 µm, whereas, Fig. 7(c) shows the external coupling, with a wavelength of 4.53 µm. It could also be used to explain that when D is less than 1, there is an interaction between the surface structure and the embedded structure. The smaller the D, the greater the influence of the surface structure on the internal coupling. In summary, when D is less than 1 µm, there is mutual coupling between the embedded structures, and between the surface structure and the embedded structure. However, when D is greater than 1 µm, the LWIR absorption does not change, and only the interaction between the embedded structures changes. Only when D is equal to 1 µm, no interaction exists.
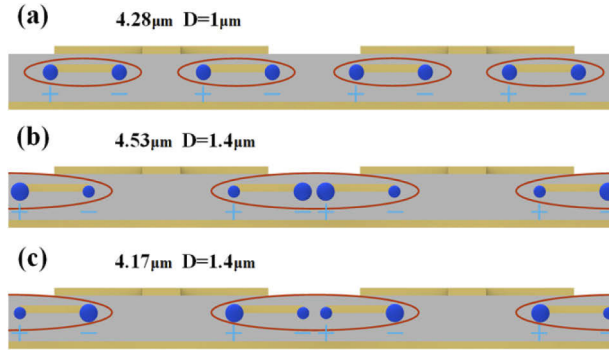
Fig. 7. Four-dipole polarization resonance model: (a) $D = 1$ μm and (b, c) $D = 1.4$ μm.
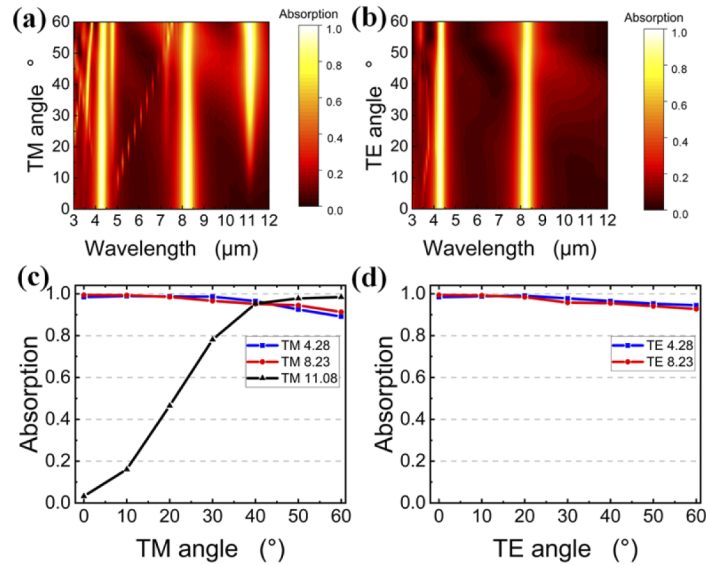

Fig. 8. The influence of the incident angle on absorption under the TM mode, and the TE mode and absorption of different angles for absorption peaks.

3.4. Impact of the incidence angle on absorption

The stability of the incidence angle is important and often overlooked when the proposed metamaterial absorbers are integrated with detectors to form imaging systems. Figure 8(a) and (b) shows the sensitivity of the absorption characteristics of the absorber to the incident angle in the TM and TE polarization modes, respectively. In the TE and TM modes, when the angle of incidence was changed at an interval of 5° from 0° to 60°, no change in the absorption peak position at 4.28 μm in the MWIR band and 8.23 μm in the LWIR band was observed. Figure 8(c) and (d) show that the absorption at the absorption peak was greater than 89%. In the TM mode, When the angle of incidence increases, a strong absorption occurred at 11.1 μm in the LWIR band. The absorption of the absorption peak increased from 16.1% when the incident angle is 10° to 98.4% when the incident angle was 60°. When the incident angle increases, a waveguide is formed between the ECS and the SCS, limiting the incident energy of the dielectric between the surface structure and the embedded structure. However, only the TM polarization mode could

excite the surface plasmon; hence, no waveguide absorption was observed with the change of the incident angle in the TE wave.

4. Conclusion

In this paper, a sub-wavelength CCS was introduced to realize a dual-band metamaterial absorber for the MWIR and LWIR bands. The absorber achieved near-unity absorption values of 98.2% and 99.5% at 4.28 μm in the MWIR band and at 8.23 μm in the LWIR, respectively. Based on the investigation of the electromagnetic-field distribution, it was observed that the high absorption was caused by the excitation of the surface plasmon. The LWIR absorption was generated by the LSP resonance of the cross structure on the surface, and the absorption of the MWIR band was mainly related to the ECS. The SCS shows a narrow-band absorption peak at 4.29 μm in the MWIR band due to the PSP resonance, and its absorption characteristics were mainly related to the insulator thickness and the structure period. The structure exhibited good modulation characteristics. By modulating the structural feature sizes, the absorption corresponded to regular changes. The change in the center distance *D* affected the interaction between the surface structure and the embedded structure. In this article, the analysis was carried out by using the quadrupole model. Besides, on increasing the incidence angle of TE and TM modes, the absorption at 4.28 μm in the MWIR band and 8.23 μm in the LWIR band hardly changed. In the TM mode, when the incidence angle was increasing, the SCS and the ECS form a waveguide, which realizes absorption at 11.08 μm in the LWIR band, and its absorption increases with an increase incidence angle.

Disclosures. The authors declare no conflicts of interest.

Data availability. Data underlying the results presented in this paper are available in Ref. [33] and [34].

References

1. J. Rensberg, Y. Zhou, S. Richter, C. Wan, S. Zhang, P. Schöppe, R. Schmidt-Grund, S. Ramanathan, F. Capasso, M. A. Kats, and C. Ronning, "Epsilon-Near-Zero Substrate Engineering for Ultrathin-Film Perfect Absorbers," Phys. Rev. A **8**(1), 014009 (2017).
2. G. Duan, J. Schalch, X. Zhao, J. Zhang, R. D. Averitt, and X. Zhang, "Identifying the perfect absorption of metamaterial absorbers," Phys. Rev. B **97**(3), 035128 (2018).
3. C. Livache, B. Martinez, N. Goubet, C. Greboval, J. Qu, A. Chu, S. Royer, S. Ithurria, M. G. Silly, B. Dubertret, and E. Lhuillier, "A colloidal quantum dot infrared photodetector and its use for intraband detection," Nat. Commun. **10**(1), 2125 (2019).
4. G. Palermo, G. E. Lio, M. Esposito, L. Ricciardi, M. Manoccio, V. Tasco, A. Passaseo, A. De Luca, and G. Strangi, "Biomolecular Sensing at the Interface between Chiral Metasurfaces and Hyperbolic Metamaterials," ACS Appl. Mater. Interfaces **12**(27), 30181–30188 (2020).
5. Y. Wang, J. Wang, X. Luo, L. Xie, S. Zhan, J. Kim, X. Wang, X. Liu, and Y. Ying, "Wearable plasmonic-metasurface sensor for noninvasive and universal molecular fingerprint detection on biointerfaces," Sci. Adv. **7**(4), eabe4553 (2021).
6. D. G. Baranov, Y. Xiao, I. A. Nechepurenko, A. Krasnok, A. Alu, and M. A. Kats, "Nanophotonic engineering of far-field thermal emitters," Nat. Mater. **18**(9), 920–930 (2019).
7. L. Long, S. Taylor, and L. Wang, "Enhanced Infrared Emission by Thermally Switching the Excitation of Magnetic Polariton with Scalable Microstructured VO$_2$ Metasurfaces," ACS Photonics **7**(8), 2219–2227 (2020).
8. F. B. Barho, F. Gonzalez-Posada, M. Bomers, A. Mezy, L. Cerutti, and T. Taliercio, "Surface-Enhanced Thermal Emission Spectroscopy with Perfect Absorber Metasurfaces," ACS Photonics **6**(6), 1506–1514 (2019).
9. A. Krishna, J. M. Kim, J. Leem, M. C. Wang, S. Nam, and J. Lee, "Ultraviolet to Mid-Infrared Emissivity Control by Mechanically Reconfigurable Graphene," Nano Lett. **19**(8), 5086–5092 (2019).
10. N. Lee, T. Kim, J. S. Lim, I. Chang, and H. H. Cho, "Metamaterial-Selective Emitter for Maximizing Infrared Camouflage Performance with Energy Dissipation," ACS Appl. Mater. Interfaces **11**(23), 21250–21257 (2019).
11. Z. Xuan, J. Li, Q. Liu, F. Yi, S. Wang, and W. Lu, "Artificial Structural Colors and Applications," The Innovation **2**(1), 100081 (2021).

12. T. Hu, Q. Zhong, N. Li, Y. Dong, Z. Xu, Y. H. Fu, D. Li, V. Bliznetsov, Y. Zhou, K. H. Lai, Q. Lin, S. Zhu, and N. Singh, "CMOS-compatible a-Si metalenses on a 12-inch glass wafer for fingerprint imaging," Nanophotonics **9**(4), 823–830 (2020).

13. M. Plidschun, H. Ren, J. Kim, R. Forster, S. A. Maier, and M. A. Schmidt, "Ultrahigh numerical aperture meta-fibre for flexible optical trapping," Light: Sci. Appl. **10**(1), 57 (2021).

14. X. Liu, T. Tyler, T. Starr, A. F. Starr, N. M. Jokerst, and W. J. Padilla, "Taming the blackbody with infrared metamaterials as selective thermal emitters," Phys. Rev. Lett. **107**(4), 045901 (2011).

15. N. I. Landy, S. Sajuyigbe, J. J. Mock, D. R. Smith, and W. J. Padilla, "Perfect metamaterial absorber," Phys. Rev. Lett. **100**(20), 207402 (2008).

16. C. M. Watts, X. Liu, and W. J. Padilla, "Metamaterial electromagnetic wave absorbers," Adv. Mater. **24**(23), OP98–OP120 (2012).

17. X. Chen, W. Li, Z. Wu, Z. Zhang, and Y. Zou, "Origami-based microwave absorber with a reconfigurable bandwidth," Opt. Lett. **46**(6), 1349–1352 (2021).

18. J. W. Rao, Y. T. Zhao, Y. S. Gui, X. L. Fan, D. S. Xue, and C. M. Hu, "Controlling Microwaves in Non-Hermitian Metamaterials," Phys. Rev. A **15**(2), L021003 (2021).

19. Z. Song, A. Chen, and J. Zhang, "Terahertz switching between broadband absorption and narrowband absorption," Opt. Express **28**(2), 2037–2044 (2020).

20. C. Du, D. Zhou, H. H. Guo, Y. Q. Pang, H. Y. Shi, W. F. Liu, J. Z. Su, C. Singh, S. Trukhanov, A. Trukhanov, L. Panina, and Z. Xu, "An ultra-broadband terahertz metamaterial coherent absorber using multilayer electric ring resonator structures based on anti-reflection coating," Nanoscale **12**(17), 9769–9775 (2020).

21. X. Cheng, R. Huang, J. Xu, and X. Xu, "Broadband Terahertz Near-Perfect Absorbers," ACS Appl. Mater. Interfaces **12**(29), 33352–33360 (2020).

22. M. Yang, X. Yan, Z. Zhang, J. Gao, L. Liang, X. Guo, J. Li, D. Wei, M. Wang, Y. Ye, X. Song, H. Zhang, Y. Ren, X. Ren, and J. Yao, "Ultra-Wideband Low-Loss Control of Terahertz Scatterings via an All-Dielectric Coding Metasurface," ACS Appl. Electron. Mater. **2**(4), 1122–1129 (2020).

23. R. L. Paldi, X. Sun, X. Wang, X. Zhang, and H. Wang, "Strain-Driven In-plane Ordering in Vertically Aligned ZnO-Au Nanocomposites with Highly Correlated Metamaterial Properties," ACS Omega **5**(5), 2234–2241 (2020).

24. K. Ou, F. Yu, G. Li, W. Wang, A. E. Miroshnichenko, L. Huang, P. Wang, T. Li, Z. Li, X. Chen, and W. Lu, "Mid-infrared polarization-controlled broadband achromatic metadevice," Sci. Adv. 6, **6**(37), eabc0711 (2020).

25. V. Nagal, T. Li, J. B. Khurgin, and D. H. Gracias, "Large-Area Arrays of Quasi-3D Au Nanostructures for Polarization-Selective Mid-Infrared Metasurfaces," ACS Appl. Nano Mater. **3**(7), 7029–7039 (2020).

26. K. Zhou, Q. Cheng, L. Lu, B. Li, J. Song, and Z. Luo, "Dual-band tunable narrowband near-infrared light trapping control based on a hybrid grating-based Fabry-Perot structure," Opt. Express **28**(2), 1647–1656 (2020).

27. J. Kim, H. Oh, B. Kang, J. Hong, J.-J. Rha, and M. Lee, "Broadband Visible and Near-Infrared Absorbers Implemented with Planar Nanolayered Stacks," ACS Appl. Nano Mater. **3**(3), 2978–2986 (2020).

28. N. Zhang, D. Cheng, X. Weng, J. Xie, and L. Deng, "Dual-band absorption of mid-infrared metamaterial absorber based on distinct dielectric spacing layers," Opt. Lett. **38**(7), 1125–1127 (2013).

29. L. Zhao, H. Liu, Z. He, and S. Dong, "Theoretical design of twelve-band infrared metamaterial perfect absorber by combining the dipole, quadrupole, and octopole plasmon resonance modes of four different ring-strip resonators," Opt. Express **26**(10), 12838–12851 (2018).

30. H. Li, A. Mekawy, and A. Alu, "Beyond Chu's Limit with Floquet Impedance Matching," Phys. Rev. Lett. **123**(16), 164102 (2019).

31. D. R. Smith, P. Markos, and C. M. Soukoulis, "Determination of effective permittivity and permeability of metamaterials from reflection and transmission coefficients," Phys. Rev. B **65**(19), 195104 (2002).

32. D. R. Smith, D. C. Vier, T. Koschny, and C. M. Soukoulis, "Electromagnetic parameter retrieval from inhomogeneous metamaterials," Phys. Rev. E **71**(3), 036617 (2005).

33. E. D. Palik, *Handbook of Optical Constants of Solids* (Academic, 1985).

34. E. D. Palik, *Handbook of Optical Constants of Solids* (Academic, 1991).

35. C. Lian, S. Q. Hu, J. Zhang, C. Cheng, Z. Yuan, S. Gao, and S. Meng, "Integrated Plasmonics: Broadband Dirac Plasmons in Borophene," Phys. Rev. Lett. **125**(11), 116802 (2020).

36. Y. Zhang, C. Min, X. Dou, X. Wang, H. P. Urbach, M. G. Somekh, and X. Yuan, "Plasmonic tweezers: for nanoscale optical trapping and beyond," Light: Sci. Appl. **10**(1), 59 (2021).

37. Y. Xu, P. Bai, X. Zhou, Y. Akimov, C. E. Png, L. K. Ang, W. Knoll, and L. Wu, "Optical Refractive Index Sensors with Plasmonic and Photonic Structures: Promising and Inconvenient Truth," Adv. Opt. Mater **7**(9), 1801433 (2019).